Observations and Modeling of Banded Orographic Convection

DANIEL J. KIRSHBAUM AND DALE R. DURRAN

Department of Atmospheric Sciences, University of Washington, Seattle, Washington

(Manuscript received 17 March 2004, in final form 6 September 2004)

ABSTRACT

Radar images and numerical simulations of three shallow convective precipitation events over the Coastal Range in western Oregon are presented. In one of these events, unusually well-defined quasi-stationary banded formations produced large precipitation enhancements in favored locations, while varying degrees of band organization and lighter precipitation accumulations occurred in the other two cases. The difference between the more banded and cellular cases appeared to depend on the vertical shear within the orographic cap cloud and the susceptibility of the flow to convection upstream of the mountain. Numerical simulations showed that the rainbands, which appeared to be shear-parallel convective roll circulations that formed within the unstable orographic cap cloud, developed even over smooth mountains. However, these banded structures were better organized, more stationary, and produced greater precipitation enhancement over mountains with small-scale topographic obstacles. Low-amplitude random topographic roughness elements were found to be just as effective as more prominent subrange-scale peaks at organizing and fixing the location of the orographic rainbands.

1. Introduction

Banded convection is a striking feature of the atmosphere that occurs in various different settings, including cloud "streets" in convective boundary layers, as well as squall lines and narrow frontal rainbands in midlatitude cyclones. Recent studies have demonstrated that rainbands may also develop in shallow potentially unstable orographic clouds. Through detailed analysis of two orographic rain events in the Cévennes region of France, Miniscloux et al. (2001) showed that after removing the portion of the total precipitation associated with propagating mesoscale disturbances, a smaller "static" component remained that appeared to be linked to the underlying topography. Subsequent numerical studies by Cosma et al. (2002) and Anquetin et al. (2003) suggest that these bands are formed by lee-side convergence around isolated peaks and ridges. The strength of the topographic relief required to form such bands was not explicitly investigated, but the idealized numerical simulations presented in Cosma et al. (2002), in which bands developed in the lee of a 1.2-km-high peak, suggest that those topographic features capable of generating bands may need to be rather large.

In contrast, Yoshizaki et al. (2000) presented two sets of radar observations of orographically generated rainbands downstream of hills over western Kyushu, Japan, in which the bands themselves dominated the total rainfall signature. Numerical simulations of one of these events demonstrated that at least one of the bands was forced by relatively modest peaks between 300 and 400 m high. Additional numerical simulations suggested that band development is favored when the topography is located in a region of mesoscale convergence within the larger-scale flow and when there is strong low-level vertical wind shear.

A somewhat different perspective on the generation of rainbands is suggested by the numerical simulations of Kirshbaum and Durran (2004, hereafter KD04), who found that convective bands could develop parallel to vertically sheared flow over a smooth ridge when the moist Brunt–Väisälä frequency within the cap cloud is negative. The individual bands of that study were triggered by small random temperature perturbations rather than isolated topographic features, and the overall character of the flow was reminiscent of boundary layer rolls (e.g., Fig. 3a of Weckwerth et al. 1997). In particular, the bands appeared to be the response to a fluid dynamical instability that developed throughout the orographic cap cloud. It is unclear whether the bands simulated by KD04 are related to the previous observations of Miniscloux et al. (2001) and Yoshizaki et al. (2000). The precipitating systems observed in Cévennes, in which the stationary component represented only a small portion of the total rainfall, were clearly more complex than simple convective roll vortices. Those in Kyushu seem closer to the type of roll

Corresponding author address: Daniel J. Kirshbaum, NCAR/MMM, P.O. Box 3000, Boulder, CO 80307-3000.
E-mail: kirshbau@ucar.edu

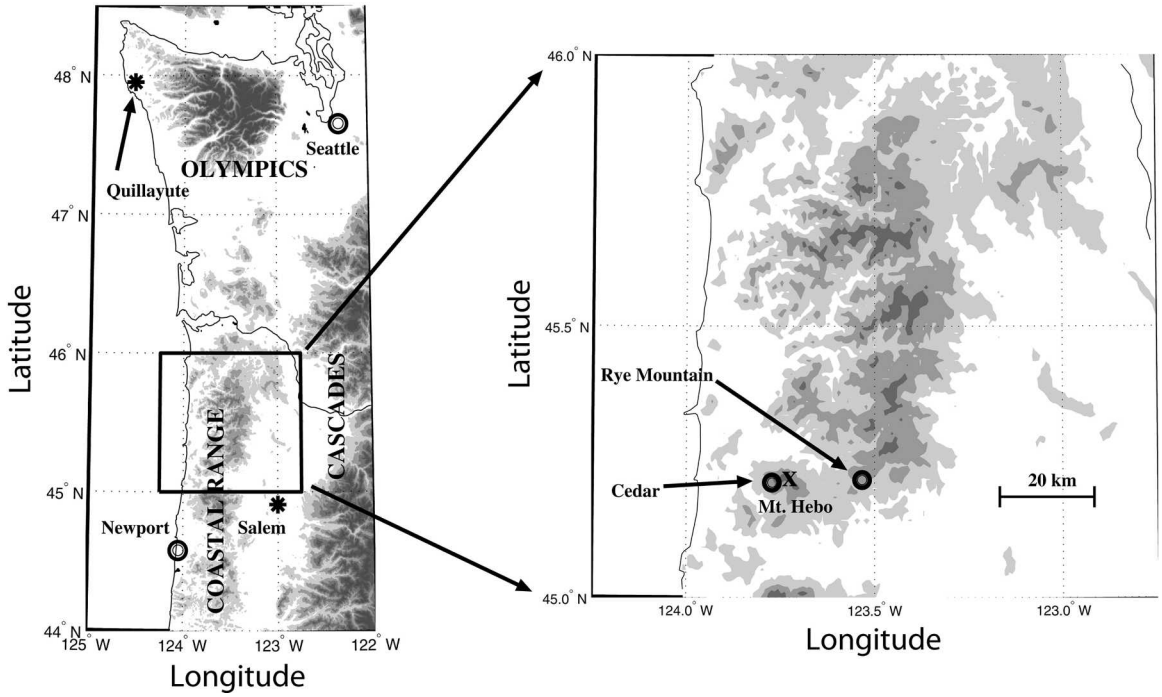

FIG. 1. Topography of Pacific Northwest and Coastal Range, shown at 250-m intervals. Circles indicate locations of surface data stations; asterisks denote radiosonde sites.

circulations that might arise in a sheared unstable fluid, but these features were more isolated and irregular than those often observed in the boundary layer or simulated by KD04. Moreover, the locations of the rainbands in Kyushu were apparently aligned with preexisting patterns of mesoscale convergence that were not present in the uniform upstream flows considered by KD04.

Additional banded orographic precipitation events were recently observed by operational weather radar over the Coastal Range in western Oregon (see Fig. 1). In this paper we will examine three cases of shallow orographic convection over these mountains. In one of these events, at least seven clearly defined bands persisted over the region for several hours. In a different case, the convection did not organize into distinct bands. In a third case, well-defined bands were present only for a couple of hours. The observations of these events are complemented by quasi-idealized numerical simulations that help illuminate the factors responsible for the differences in convective organization observed in the three cases. A more extensive analysis of the fundamental dynamics governing these bands will be presented in a subsequent paper (Kirshbaum and Durran 2005).

2. Observations of banded convection

Three convective precipitation events occurred over the Oregon Coastal Range on 9–10 April 2002, 12–13 November 2002, and 12 October 2003; throughout the subsequent analysis these events will be referred to as Case 1, Case 2, and Case 3, respectively. All three cases developed in similar synoptic settings, following the passage of mature surface cold fronts that had traveled for great distances over the Pacific Ocean. Because of their prolonged exposure to relatively warm ocean waters, the postfrontal air masses were warmed and moistened near the surface. By the time they made landfall on the west coast of North America, these air masses had developed considerable amounts of potential instability in the layer from the surface to about 750 mb. Shallow clouds and convective precipitation were produced as the potentially unstable air was lifted over the Coastal Range.

a. Correlation between the precipitation and the underlying topography

The convective organization in the three precipitation events under consideration is shown in Fig. 2 by 0.5°-elevation radar images from the Portland, Oregon, Next-Generation Weather Radar (NEXRAD) site, which has a nominal horizontal resolution of 1 km and is located approximately 60 km northeast of the center of the Coastal Range at an elevation of 541 m above sea level. To show the relationship between the precipitation and the underlying topography, contours of radar reflectivity data, smoothed by a nine-point spatial filter, are overlaid upon shaded 250-m contours of the topography. Two images for each case are presented approxi-

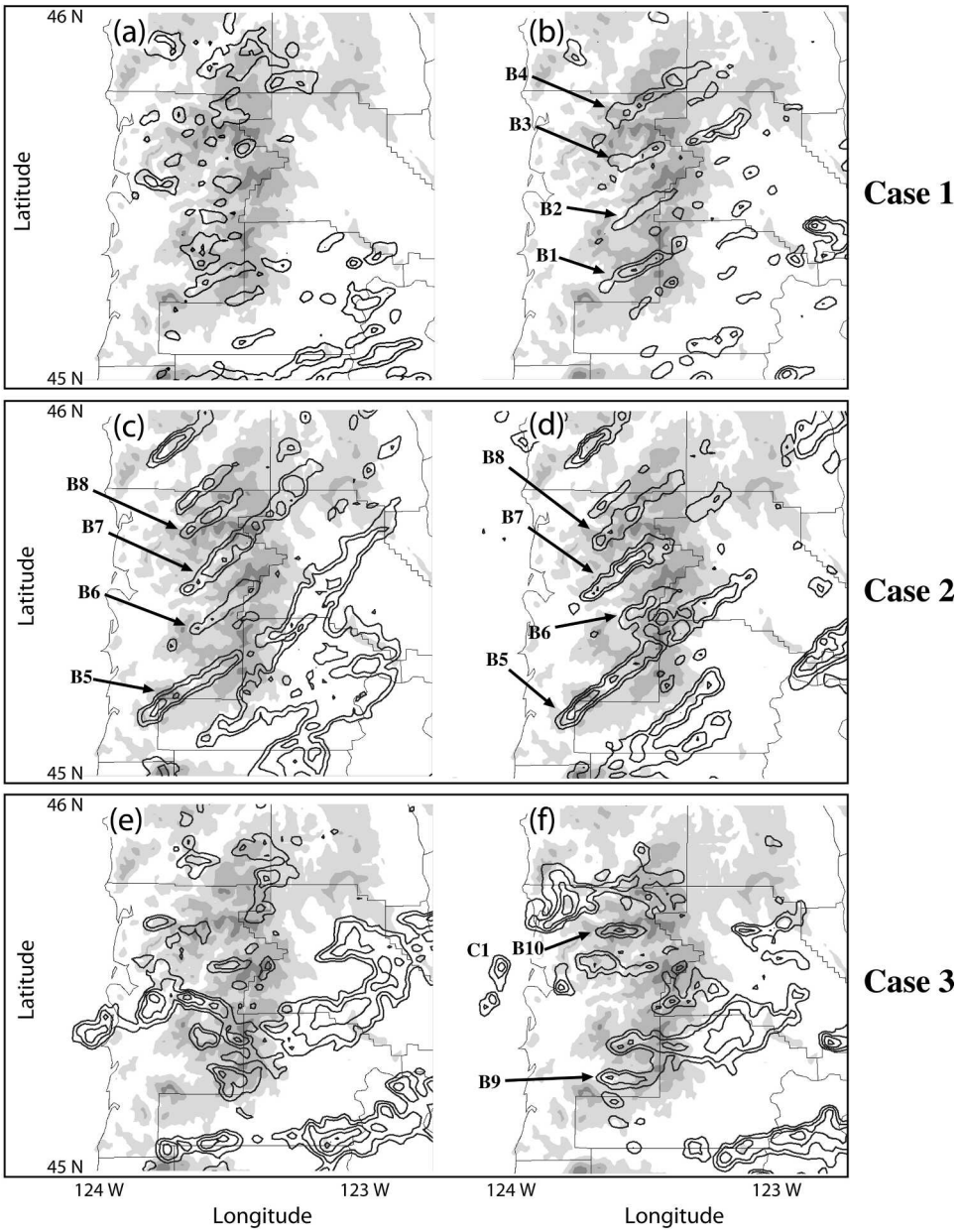

FIG. 2. Portland, OR, NEXRAD images at 0.5° elevation for three cases of convective precipitation over Coastal Range topography. Case 1 at (a) 2316 UTC 9 Apr 2002 and (b) 0017 UTC 10 Apr 2002; Case 2 at (c) 2003 UTC 12 Nov 2002 and (d) 2102 UTC 12 Nov 2002; Case 3 at (e) 1856 UTC 12 Oct 2003 and (f) 2000 UTC 12 Oct 2003. Contour interval for grayscale topography is 250 m; contour interval for overlaid radar images is 10 dB*Z*.

mately 1 h apart to illustrate the time evolution of convective rainfall during these events. The precipitation exhibited varying degrees of organization, with Case 2 (Figs. 2c,d) clearly displaying the most organized and robust-banded structures.

The precipitating structures in Case 1, which developed after the passage of a surface cold front at approximately 2200 UTC on 9 April 2002 and continued for over five hours, are apparent from the contoured radar images at 2316 UTC on 9 April 2002 and 0017 UTC on 10 April 2002 shown in Figs. 2a,b. Observed rainfall areas over the Coastal Range varied in structure from disorganized cells (Fig. 2a) to linearly oriented bands (Fig. 2b). Rainbands such as those seen in Fig. 2b developed repeatedly over the elevated terrain from 2330 to 0240 UTC and propagated downstream with the southwesterly flow. After advecting into the lee of the Coastal Range, the bands were replaced by

fresh convection on the upslope, in some cases forming over nearly identical locations as the previous bands. Although bands B1 and B2 in Fig. 2b formed directly downstream of isolated small-scale peaks, other bands (e.g., B4) were not associated with peaks, and band B3 even appears over a valley.

During Case 2, unusually well-defined banded structures formed in the postfrontal southwesterly flow over the Coastal Range at approximately 1900 UTC on 12 November 2002 and persisted for eight hours in a quasi-stationary pattern. The similarities between contoured radar plots at 2003 and 2102 UTC on 12 November 2002 in Figs. 2c,d is characteristic of the remarkable steadiness of the convective bands in this event. The locations of rainbands labeled B5, B6, B7, and B8 in Fig. 2c were nearly identical one hour later (Fig. 2d); these bands persisted in similar locations throughout this entire precipitation event. As in Case 1, some of the bands (e.g., B5 and B6) were located above or downstream of isolated peaks, while others could not be clearly tied to small-scale topographic obstacles. Note that the locations of bands B5–B8 are nearly identical to that of B1–B4 in Case 1 (Fig. 2b), indicating that these particular bands may have been linked to the same topographic features. The intensity and stationarity of the rainbands in this event resulted in dramatic small-scale variability in the eight-hour cumulative precipitation. For example, the observation sites of Cedar and Rye Mountain, which are shown in Fig. 1 to lie about 20 km apart in the east–west direction, experienced vastly different amounts of rainfall. Cedar, positioned on the upslope of Mt. Hebo (965 m) directly under precipitation band B4, recorded a maximum hourly rainfall accumulation of 19 mm and an 8-h accumulation of 69 mm, while Rye Mountain received only 3 mm of total precipitation. By contrast, the precipitation accumulations were very light (less than 9 mm) and did not vary significantly between these same two locations in Cases 1 and 3.

Case 3 occurred in postfrontal flow over the Coastal Range from 1500 to 2300 UTC on 12 October 2003, and exhibited more westerly low-level flow with far less organized precipitation than in the other cases. Radar reflectivities at 1856 and 2000 UTC on 12 October 2003 (Figs. 2e and 2f, respectively) reveal some poorly organized bands (e.g., B9 and B10 in Fig. 2f) over the mountain, along with more cellular structures (e.g., C1) that formed primarily in the flow upstream of the Coastal Range and intensified while advecting eastward over the elevated terrain. Although some rainbands, such as B9 and B10, did appear to form in the vicinity of small-scale topographic peaks as in Cases 1 and 2, they lasted for shorter periods and were much less elongated than the orographic bands in the previous cases. Despite the comparable radar reflectivities and precipitation coverage apparent between Cases 2 and 3, the rainfall measured at both Rye Mountain and Cedar was much greater in Case 2.

b. Detailed structure of precipitation bands

The radar reflectivity images in Fig. 2 show precipitating structures that varied substantially between Cases 1, 2, and 3. Because this radar data has been smoothed and contoured at 10-dBZ intervals, however, some of the more subtle features in the precipitation fields may not be evident. To more closely compare the properties of the precipitation bands in the three cases, grayscale images of the raw radar data are plotted in Fig. 3. An example of the additional accuracy and detail provided by the raw data may be seen by comparing Figs. 2b and 3a, which correspond to the same observation time. While only four rainbands are apparent in the smoothed contour plot (Fig. 2b), the raw data in Fig. 3a shows at least seven bands, allowing for a more accurate measure of the spacing and finescale structure of these features.

Estimates of the mean orientation, width, and spacing of the convective bands, as well as maximum radar reflectivities over the Coastal Range, are provided in Table 1. Mean spacings could only be determined for the well-organized precipitation bands of Cases 1 and 2; the bands in Case 3 were too isolated for a representative value to be estimated. The quasi-steady precipitation bands in Case 2 possessed the largest average bandwidths (4 km) and spacings (8 km), while the more disorganized convective structures in Case 3 had the highest maximum radar reflectivities (50 dBZ). Convective bands in Case 1, though well organized, had the shortest horizontal scales and weakest maximum reflectivities.

3. The upstream flow

Vertical sounding profiles upstream of the Oregon Coastal Range serve two important purposes in this study: first, the basic-state atmospheric structures yield valuable insight into the dynamical behavior of the flows under consideration; second, these profiles function as inflow boundary conditions for the quasi-idealized numerical simulations to be discussed in section 4. The determination of soundings upstream of the Coastal Range, however, is complicated by the fact that this region lies over the open ocean where no instrumentation exists to gather sounding data. A best-guess estimate of the upstream conditions is therefore created from soundings collected at Salem, Oregon (see Fig. 1), by adjusting the low-level wind and thermodynamic variables to account for Salem's location on the lee side of the Coastal Range.

a. Thermodynamic profiles

Table 2 compares low-level temperatures (T), relative humidities (RH), and equivalent potential temperatures (θ_e) at the four Pacific Northwest locations indicated in Fig. 1. These data give surface and 850-mb

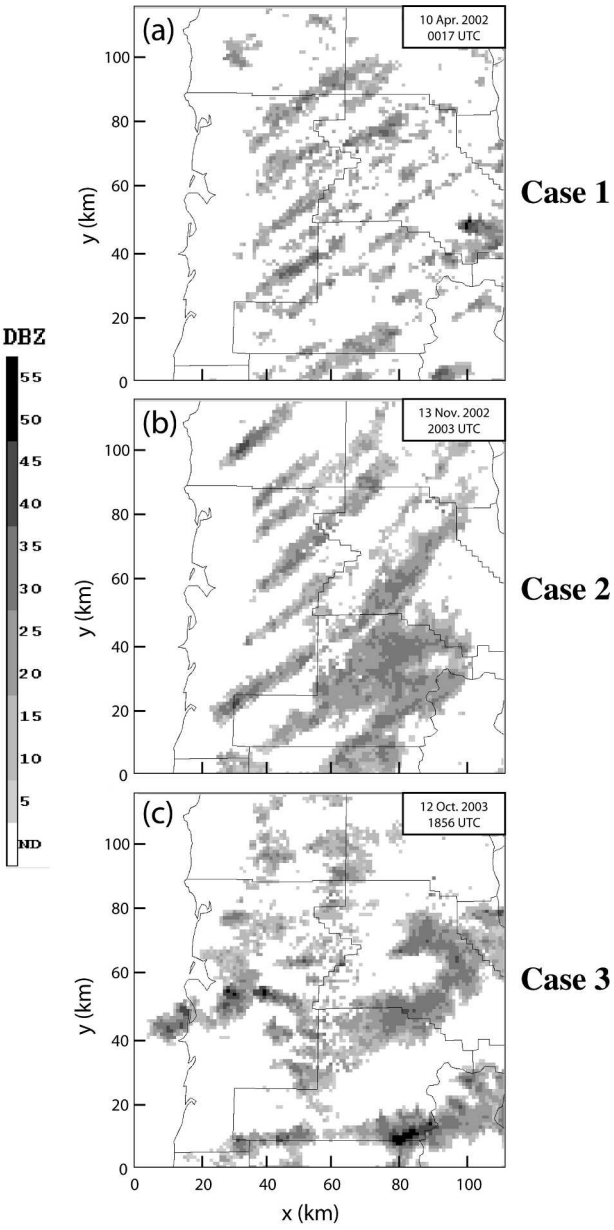

FIG. 3. Grayscale images of raw Portland, OR, NEXRAD 0.5° elevation data for (a) Case 1, 0017 UTC 10 Apr 2002; (b) Case 2, 2003 UTC 12 Nov 2002; (c) Case 3, 1856 UTC 12 Oct 2003.

radiosonde data from Salem and Quillayute, Washington, as well as surface measurements from Newport, Oregon, and Seattle, Washington. The best available times for radiosonde soundings in these cases are 0000 UTC on 10 April 2002 (Case 1), 0000 UTC on 13 November 2002 (Case 2), and 0000 UTC 13 October 2002 (Case 3). For consistency, the surface measurements from Newport and Seattle are provided at the same times. According to Table 2, the surface relative humidities at the coastal locations (Newport and Quillayute) are very similar for all three cases and much larger than the values further inland (Salem and Seattle). These west-to-east gradients in near-surface relative humidities, however, are not reflected in the equivalent potential temperatures; surface θ_e values in Table 2 are similar between Salem and Newport, as well as between Quillayute and Seattle. The differences in relative humidity between coastal and inland locations apparent at low levels are considerably reduced at higher elevations, as evidenced by the comparatively similar 850-mb humidities at Quillayute and Salem in Table 2. In addition, the vertical gradients of θ_e between the surface and 850 mb are consistent between Salem and Quillayute, suggesting that the low-level θ_e profiles have similar structure on either side of the coastal mountains.

From the above comparison it may be concluded that radiosonde data at Salem, while providing accurate estimates of the θ_e values upstream of the Coastal Range, do not reflect the high values of relative humidity observed at coastal locations. Thus, to generate upstream soundings that better represent conditions in the upstream flow, we have replaced humidity values from the Salem sounding in the surface to 850-mb layer with representative values from Quillayute (at identical times and linearly interpolated to represent the same elevations). A constant value of 90% was used over this layer for Cases 1 and 2, which was within 5% of the values measured at Quillayute, while values interpolated directly from the Quillayute sounding were used in Case 3 because of its comparatively large variations in humidity with height. An iterative procedure was then used to solve for the proper values of T and water vapor mixing ratio (q_v) necessary to maintain the θ_e profile observed in the Salem sounding. The raw thermodynamic data from Salem was left unchanged above the 850-mb level, resulting in the skew-T profiles shown in Figs. 4a, 4b, and 4c for Cases 1, 2, and 3, respectively. Profiles of θ_e, compared in Fig. 5a, show that all three upstream soundings have potential instability from the surface to about $z = 2.5$ km and absolutely stable flow at higher levels. Likewise, the relative humidity profiles (Fig. 5b) are similar for the three cases, with high values (greater than 80%) between the surface and $z = 2$ km, and much lower values aloft.

b. Velocity profiles

The low-level velocity also undergoes significant modification as the flow approaches Salem from the Oregon coastline. Increased frictional dissipation over land heightens the surface stress and reduces the near-surface wind speeds as the flow moves inland. Because of the presence of the north–south-oriented Coastal Range directly to the east, low-level winds at coastal stations may be affected by upstream blocking and consequently cannot be assumed to accurately characterize the velocity in the undisturbed offshore flow. A rough estimate of the offshore conditions may, however, be inferred from short-term forecasts from numerical

TABLE 1. Comparison of precipitation properties for observed data and simulations of three precipitation events, measured from Figs. 3 and 7. Mean band alignment angle is measured counterclockwise relative to the east, mean width is defined as distance between 5-dBZ contours on the flanks of individual precipitation bands, mean spacing is distance between adjacent bands, and mean aspect ratio is quotient of horizontal lengths and widths of bands. Radar reflectivities Z are calculated in simulations from q_r values through a conversion algorithm from Douglas (1964): $Z = 2.4 \times 10^4 M^{1.82}$, where $M = \rho_{\text{dry}} q_r$.

	Observed			Simulated		
Property	Case 1	Case 2	Case 3	Case 1	Case 2	Case 3
Alignment	25°–30°	30°–35°	0°–5°	20°–25°	30°–35°	0°–5°
Mean width (km)	2	4	2	2	3	3
Mean spacing (km)	4	8	N/A	3	5	N/A
Mean aspect ratio	6	6	2.5	7.5	7	3
Max reflectivity (dBZ)	30	35	50	35	45	50

weather prediction models. Here we use 12-h forecasts from the nonhydrostatic fifth-generation Pennsylvania State University–National Center for Atmospheric Research (Penn State–NCAR) Mesoscale Model (MM5) to obtain predictions for surface velocities off the northwestern Oregon coast. These simulations were performed at the University of Washington over the Pacific Northwest at 12-km horizontal resolution using boundary conditions from the National Centers for Environmental Prediction (NCEP) global forecast system (GFS) global model. MM5 predictions were combined with upper-level data from the Salem soundings to better represent upstream wind conditions in the three events. To smoothly connect the model and sounding data, the winds in the lowest kilometer are linearly interpolated between the MM5 surface values and the values observed at $z = 1$ km in the Salem soundings. The zonal flow (U) is westerly in all three cases and increases with height (Fig. 5c), whereas the meridional flow (V) exhibits considerable variability between the three cases.

4. Quasi-idealized numerical simulations

In this section we explore whether the precipitating structures seen in the radar data (Fig. 2) can be qualitatively captured in quasi-idealized simulations. These simulations are quasi-idealized in that they combine a reasonable approximation to the large-scale atmospheric flow during each event with a simplified topographic profile. The simplified topography is superior to the actual topography for the purposes of testing our hypothesis that the rainbands in these events are the manifestation of a fluid dynamical instability that develops in the statically unstable orographic cap cloud. The use of a simplified topography also makes it easier to assess the influence of subridge-scale structures on the locations of the bands.

a. Experimental setup

The cloud-resolving, nonhydrostatic, fully nonlinear numerical model used in this study is described in Durran and Klemp (1983) and Epifanio and Durran (2001). This model contains a flux-limited scalar advection scheme (Leveque 1996) to eliminate spurious overshoots caused by steep spatial gradients, a subgrid-scale turbulence formulation based on Lilly (1962), and a Kessler warm-rain parameterization for cloud microphysics. Ice processes are neglected for simplicity and because the cloud tops in these events generally did not extend far above the freezing level. Because of the relatively short cross-barrier extent (~50–100 km) of the Coastal Range, the characteristic Rossby numbers of these flows are large and rotational effects have consequently been neglected. The section of the Coastal Range highlighted in Fig. 1 is represented by an idealized finite-length ridge of the form

$$h(x, y) = \begin{cases} \dfrac{h_0}{16}[1 + \cos(\pi r)]^4 & : \quad r \le 1 \\ 0 & : \text{ otherwise} \end{cases}, \qquad (1)$$

TABLE 2. Comparison of low-level thermodynamic data for three test cases: temperature (T), relative humidity (RH), and equivalent potential temperature (θ_e) provided at various locations and heights.

		Case 1 0000 UTC 10 Apr 2002			Case 2 0000 UTC 13 Nov 2002			Case 3 0000 UTC 13 Oct 2002		
Location	Height	T (K)	RH (%)	θ_e (K)	T (K)	RH (%)	θ_e (K)	T (K)	RH (%)	θ_e (K)
Salem	Surface	286.2	78	305.2	287.4	85	309.4	289.0	68	308.0
Quillayute	Surface	283.0	100	303.1	285.0	90	306.1	286.2	88	307.0
Newport	Surface	284.7	100	305.3	286.9	93	309.3	286.9	90	307.6
Seattle	Surface	284.7	83	302.7	286.3	81	305.5	287.4	72	305.7
Salem	850 mb	277.8	92	300.8	278.8	87	304.7	286.2	80	301.9
Quillayute	850 mb	273.8	88	298.4	275.0	87	300.5	275.2	92	301.6

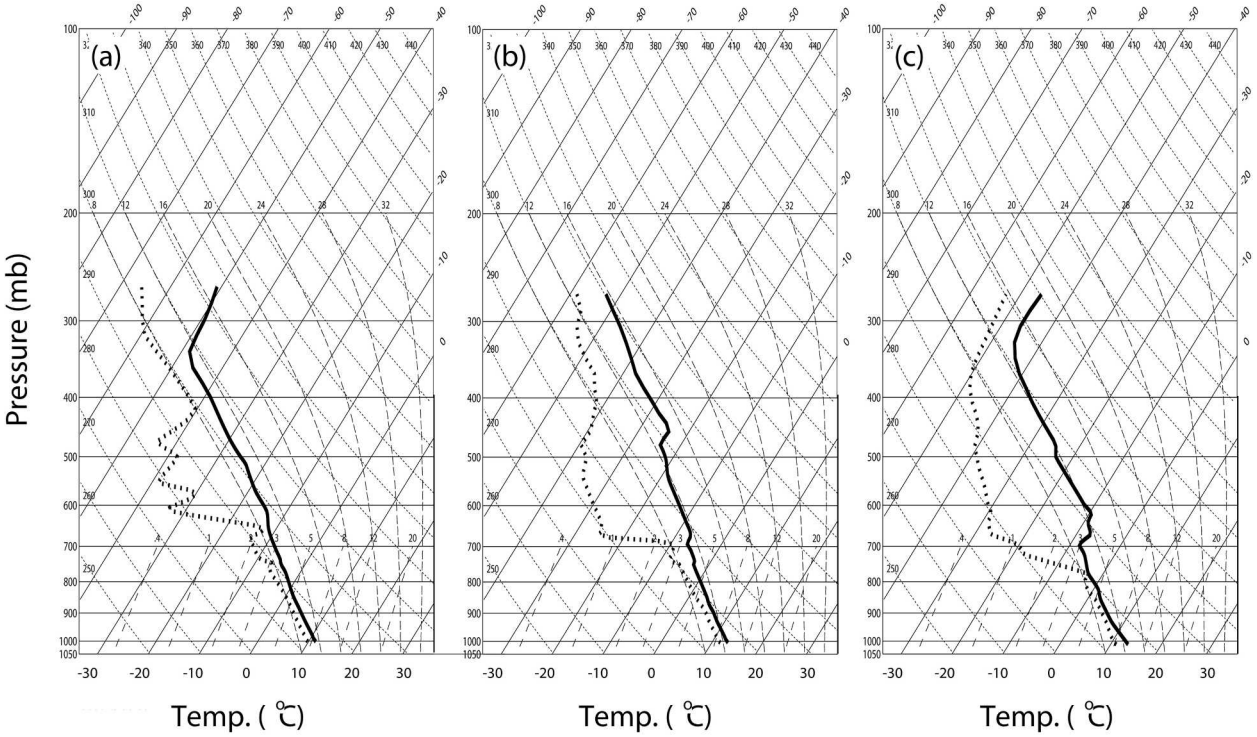

FIG. 4. Skew T–log$p$ profiles for (a) Case 1, (b) Case 2, and (c) Case 3. Temperature profiles are shown by solid line, dewpoint by dashed line.

where

$$r^2 = \begin{cases} \left(\dfrac{x - x_0}{4a}\right)^2 + \left(\dfrac{|y - y_0| - B}{4b}\right)^2 & : \ |y - y_0| > B \\ \left(\dfrac{x - x_0}{4a}\right)^2 & : \ \text{otherwise} \end{cases}. \quad (2)$$

In the preceding, $x_0 = y_0 = 225$ km, $h_0 = 1$ km, $a = 15$ km on the windward side of the mountain and 10 km on the lee, $b = 10$ km, and $B = 30$ km.

To provide high spatial resolution directly over the mountain while limiting the overall computational expense, three-level, two-way grid nesting has been employed. Figure 6 illustrates the grid configurations and terrain profile for these simulations, in which the out-

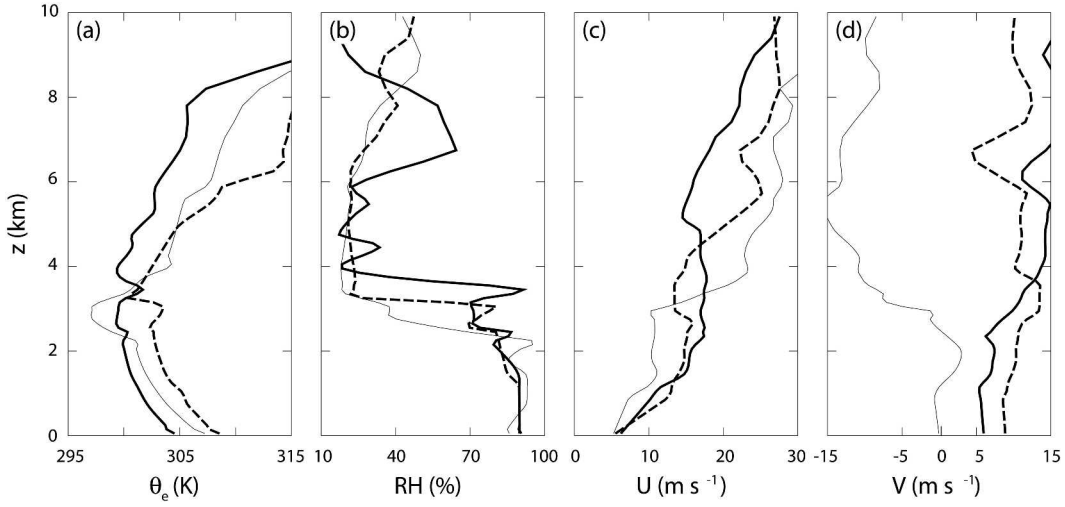

FIG. 5. Comparison of vertical profiles of (a) θ_e, (b) relative humidity, (c) zonal wind speed (U), and (d) meridional wind speed (V) for three test cases. Case 1 is given by thick solid line, Case 2 by thick dashed line, and Case 3 by thin solid line.

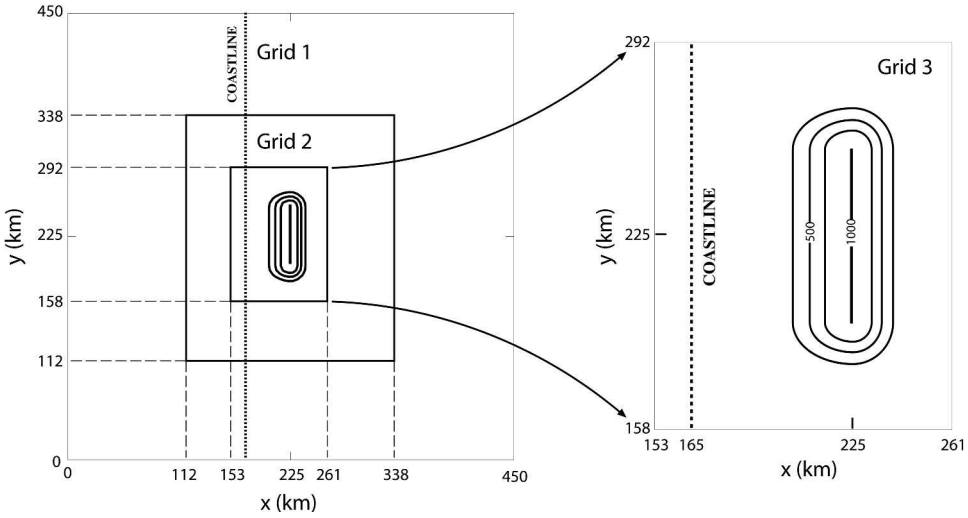

FIG. 6. Numerical domain for quasi-idealized simulations showing the grid nesting and contours of the topography at 250-m intervals.

ermost domain has dimensions of 450 km by 450 km, horizontal grid spacings (Δ) of 4.5 km, and an integration time step (Δt) of 36 s. Horizontal grid spacings are reduced to 1.5 km and 500 m on the two successively finer nested grids, with respective values of Δt reducing to 12 and 4 s. The vertical resolution (Δz) is 100 m over $0 \leq z < 5$ km, stretching linearly to 400 m over $5 \leq z < 8$ km, then remaining constant at 400 m to the top of the domain at 10 km.

The vertical profiles shown in Figs. 4 and 5 are used as upstream boundary conditions for simulations of the three different test cases. As discussed in section 3, these profiles are intended to represent offshore conditions upstream of the Coastal Range, and may be expected to change significantly as the flows encounter greater frictional dissipation over land. To capture the effects of increased surface stress over land surfaces, frictional effects are included to the east of the idealized coastline, shown in Fig. 6 by the dashed line at $x = 165$ km. Surface friction is imposed in this region through a first-order Blackadar scheme based on Zhang and Anthes (1982) in which the Monin–Obukhov similarity theory is assumed to prevail in a surface layer added to the model at $z = 10$ m. The large near-surface vertical shears forced by friction cause the Richardson number in that layer to fall below the critical value of 0.25 for dynamic instability, inducing subgrid-scale vertical mixing with adjacent layers and thereby deepening the shear layer with the passage of time. As the depth of this near-surface shear layer increases, the instability at its top eventually weakens to the point where continued upward growth of the boundary layer becomes negligible. In the simulations analyzed for this study, this quasi-steady state is generally reached after approximately three hours of integration time ($t = 10\,800$ s) with boundary layer depths approaching 500 to 600 m.

To initiate convective motions within any statically unstable regions that develop in regions of saturated flow, small-amplitude random noise is added to the initial thermal field on the finest numerical grid (labeled grid 3 in Fig. 6), and at all subsequent time steps on the upstream boundaries of that grid. This noise field is created by assigning a uniformly distributed random number to each thermodynamic grid point, filtering these values by a single application of a diffusion operator along each coordinate axis to remove all forcing at 2Δ, and then scaling the field to have a 0.1-K root-mean-squared (rms) amplitude. Convective motions were also initiated by small-amplitude irregularities on the mountainous topography. These small-scale surface bumps, which are filtered 4 times through a two-dimensional diffusion operator to remove topographic forcing at the model's least-resolvable scales, have an rms amplitude of 30 m. Note that the rms amplitude of the bumps is only 3% of the maximum mountain height (1 km).

b. Simulation results

The convective structures produced by quasi-idealized numerical simulations of Cases 1, 2, and 3 are revealed by the horizontal cross sections of the rainwater mixing ratio (q_r) displayed in Fig. 7. To allow for direct comparison with the radar images in Fig. 2, the simulation results are provided at a height of $z = 1.5$ km, representative of the level reached by the 0.5° elevation Portland NEXRAD radar beam over the Coastal Range upslope, and at two integration times separated by one hour ($t = 4$ and 5 h). By 4 h, the evolution of mesoscale processes such as boundary layer development and mountain wave formation are largely complete, and the orographic clouds develop in a steady background environment.

From inspection of Figs. 7 and 2, the simulated q_r

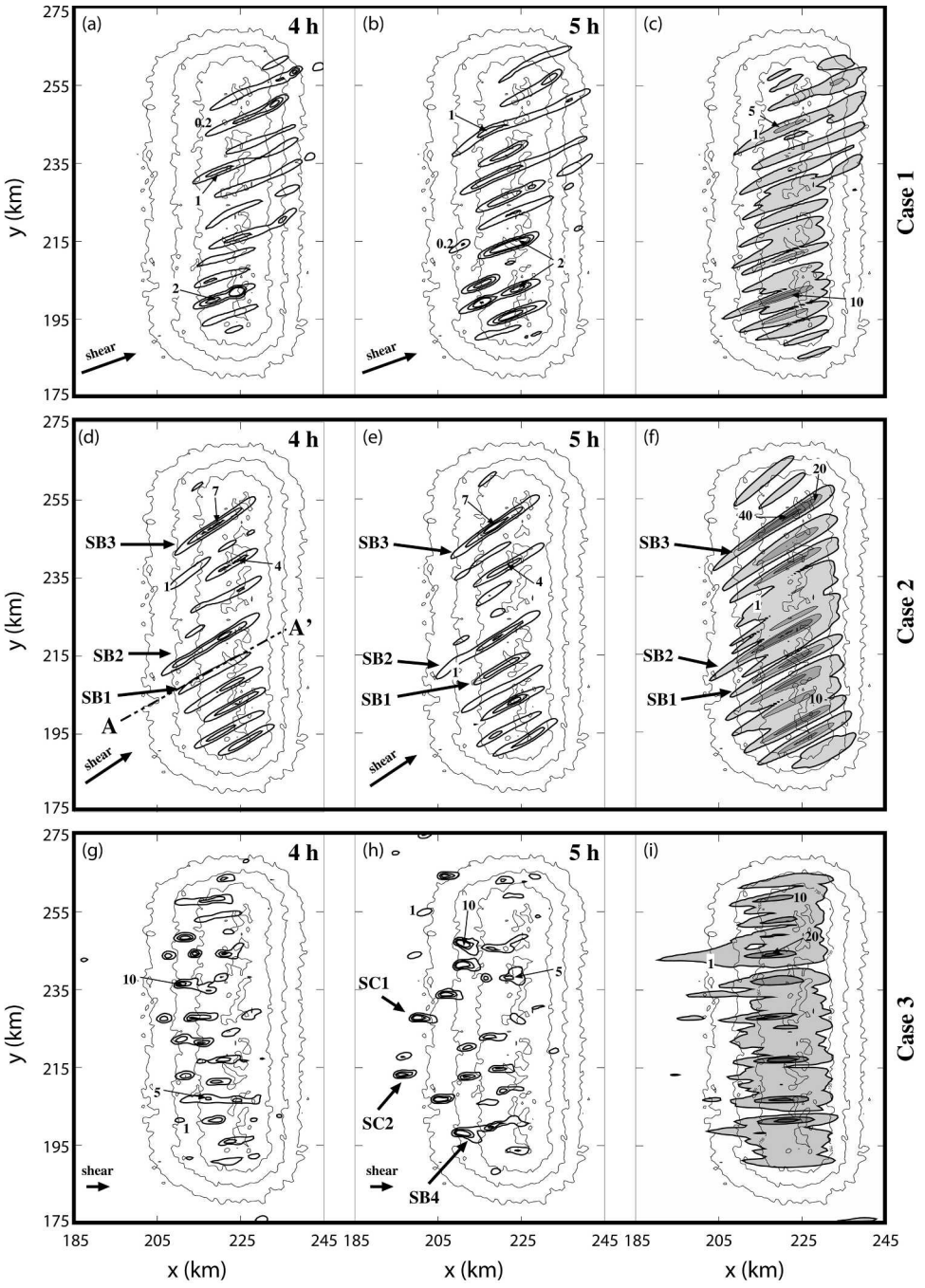

FIG. 7. Quasi-idealized simulation results over roughened topography. Rainwater mixing ratios (q_r) at (a) $t = 4$ h, (b) $t = 5$ h, and (c) cumulative precipitation at $t = 5$ h for Case 1; (d)–(f), as in (a)–(c) but for Case 2; (g)–(i) as in (a)–(c) but for Case 3. Arrows labeled "shear" indicate direction and relative magnitude of vertical shear over $0 \leq z \leq 2.5$ km. Contours of q_r are multiplied by 10^{-4}. Precipitation contours are 1, 5, and 10 mm in (c); 1, 10, 20, and 40 mm in (f); 1, 10, and 20 mm in (i). Topographic contours are in intervals of 250 m.

fields in all three cases appear qualitatively similar to the rainfall patterns observed by the radar. Moreover, the basic variations between precipitating structures in the different events are reproduced by the numerical simulations. As in the radar data, the Case-2 simulation has the most stationary and well-defined bands. Their quasi-stationary character is apparent from the nearly identical locations of bands SB1, SB2, and SB3 in Figs.

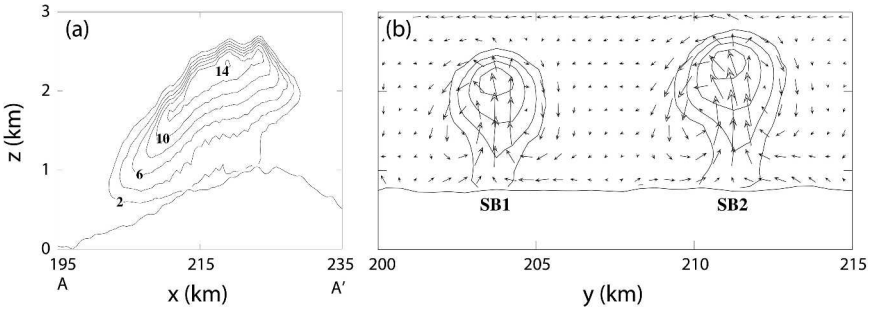

FIG. 8. Vertical cross sections of cloud liquid water (q_c) of rainband SB1 at $t = 4$ h in Fig. 7d. (a) Slice from A–A′ and (b) y–z cross section along $x = 215$ km. Labeled contours of q_c are multiplied by 10^{-4} in (a); contours are 1, 4, 8, and 12×10^{-4} in (b). Horizontal component of overlaid vectors in (b) is roll-perpendicular perturbation velocity; vertical component is w. Velocity vectors are shown at every horizontal grid point and every two vertical grid points. Vector lengths in (b) scale linearly, with a maximum value of 2.3 m s^{-1}.

7d,e, and from the banded appearance of the cumulative precipitation field in Fig. 7f. By contrast, the bands in Case 1 have lower intensities, slightly smaller horizontal scales, and reduced steadiness, as seen by the differences in the locations of the bands at $t = 4$ and 5 h (Figs. 7a,b). While the cumulative precipitation field in Case 1 (Fig. 7c) exhibits a somewhat banded structure, the precipitation is much weaker and less localized than that of Case 2. Comparatively disorganized precipitating features are apparent in the Case-3 simulation; as in the radar observations, a combination of cellular and banded structures tend to develop upstream and over the mountainous topography (Figs. 7g,h). Some cells (for example, SC1 and SC2 in Fig. 7h) form upstream of the mountain and strengthen while drifting over the elevated terrain, while both cells and banded features such as SB4 in Fig. 7h develop directly over the mountain. The disorganized cells in Case 3 produce a broad region of light precipitation over the mountain (Fig. 7i) that is enhanced in certain locations where strong cells or elongated rainbands like SB4 repeatedly develop.

A representative example of the vertical structure of the orographic rainbands in the Case-2 simulations is provided in Fig. 8. The cloud liquid water (q_c) field in a vertical slice through band SB1, along line A–A′ in Fig. 7d, is shown in Fig. 8a, indicating the relative uniformity of cloud properties along the axis of the cloud band. In Fig. 8b the q_c contours along a y–z cross section just upstream of the crest ($x = 215$ km), intersecting bands SB1 and SB2 are overlaid by vectors composed of the vertical velocity w and the horizontal velocity perturbation in the roll-perpendicular direction. The bands are clearly governed by well-defined roll-type circulations, with cloudy regions in the ascending branches of the rolls. These circulations reach heights of 2 to 3 km, representative of the depth of the moist, potentially unstable upstream layer in which the parent cap cloud forms (see Figs. 5a,b).

The basic features of radar observations and simulated data for the three test cases are quantitatively compared in Table 1. In all cases, the horizontal alignment of the convective bands is represented accurately by the numerical simulations, while the widths and spacings of the bands are slightly underestimated and maximum reflectivities slightly overestimated. Convective bands also tend to be slightly more elongated in the simulations, as seen by the modest increases in the mean aspect ratio for the three cases in Table 1. Nevertheless, the generally good agreement between the simulated and observed cloud structures suggests that the fundamental mode of convective organization is determined primarily by the upstream atmospheric state (which is accurately incorporated in each simulation) rather than the details of the topography (which are highly idealized).

The ability of numerical simulations to produce convective features with physically realistic structures and intensities—and qualitatively capture the basic differences apparent between observed cases—suggests that simulations may serve as a useful tool for evaluating the factors controlling the behavior of shallow orographic convection. One such simulation was conducted to see if the westerly wind direction played a role in reducing the bandedness in Case 3 by reducing the residence time of air parcels within the cap cloud relative to parcels following the more southwesterly trajectory evident in Cases 1 and 2. When the winds in Case 3 were rotated so that the low-level flow was from the southwest (along the same axis as in Case 2), there was no increase in the length or steadiness of the bands, although those short transient bands that did form were parallel to the new flow direction.

5. Influence of small-scale perturbations on convective structure

The radar observations presented in section 2 and numerical simulations just described in section 4 indi-

cated obvious differences in the convective behavior of the three orographic precipitation events. Cases 2 and 3 were the most different, with the former characterized by well-defined, quasi-stationary bands and the latter by disorganized and transient convective cells. To investigate the factors contributing to these differences, we first consider the specific contributions of the two different small-scale initiation mechanisms present in the simulations: thermal inhomogeneities in the flow and topographic irregularities on the mountain. Note that, in simulations performed in the absence of these initiation mechanisms (not shown), no obvious convection occurred within the orographic cap cloud. Without sufficient excitation of rapidly amplifying, submountain-scale modes, embedded convective motions remained weak in these simulations over the limited period of time that air parcels passed through the unstable orographic cloud.

a. Isolating responses to thermal and topographic perturbations

The three simulations described in section 4 are first compared with three otherwise identical simulations in which no random noise was added to the topography [leaving just the smooth mountain profile given by (1)]. Inspection of horizontal cross sections of the q_r and cumulative precipitation fields indicates that convection in the smooth-mountain cases (Fig. 9) is generally similar in both structure and intensity to that produced in cases with roughened topography (Fig. 7). Nevertheless, systematic differences are apparent in those cases that develop well-defined orographic rainbands (Cases 1 and 2). In these cases, the bands are longer and more regularly spaced over the roughened terrain (Figs. 7a–f) than over the smooth mountain (Figs. 9a–f). In addition, the randomly distributed small-scale bumps strongly increase the overall steadiness of the orographic rainbands. Convective bands that form in the smooth-topography simulations propagate downstream with the prevailing flow, continually being replaced by fresh convection in new locations on the upslope. Over roughened topography, on the other hand, rainbands such as SB1, SB2, and SB3 in Figs. 7d,e remain almost stationary for extended periods. The steadiness of the rainbands over the roughened terrain creates much more banded cumulative precipitation fields (Figs. 7c,f) with far larger precipitation maxima (15 and 43 mm, respectively) than the corresponding simulations with smooth terrain (Figs. 9c,f), in which the respective precipitation maxima are only 5 and 16 mm.

Compared with Cases 1 and 2, the differences between the convective formations in the smooth and roughened topography simulations of Case 3 are far less obvious. The convective cells that form in the flow upstream of the mountain and propagate over the orography (e.g., SC1 and SC2) tend to be randomly distributed over the mountainous terrain and are not strongly affected by small-scale terrain fluctuations. Because these cellular features dominate the rainfall pattern in Case 3, the precipitation is distributed over a much broader region than that in Cases 1 and 2, and the addition of topographic roughness produces only a modest increase in maximum precipitation (29 mm in Fig. 7i) compared to the smooth mountain simulation (23 mm in Fig. 9i).

Now consider three simulations in Fig. 10 that are identical to the original simulations in section 4 except they are initialized without thermal perturbations, leaving small-scale topographic roughness as the only mechanism for triggering the convection. Compared to the previously discussed simulations containing thermal perturbations (Figs. 7 and 9), the convection in these cases (Fig. 10) is more banded. This is especially true for Case 3, where both the q_r fields (Figs. 7g–h) and the precipitation field (Fig. 7i) are organized into distinct bands when the instabilities are triggered solely by the roughened topography. Finally note that in the absence of thermal perturbations, no convective cells form upstream of the topography; for example, cells SC1 and SC2 in Fig. 7h have no equivalent in Fig. 10h. As will be discussed further in section 6b, it appears that one factor leading to the absence of well-defined bands in Case 3 was a greater susceptibility of the atmosphere to low-level convection upstream of the mountains.

In contrast to some previous studies into the factors controlling orographic rainbands (e.g., Yoshizaki et al. 2000; Cosma et al. 2002), the above simulations indicate that small-scale topographic obstacles are not necessary for these features to form, as rainbands in Cases 1 and 2 developed even in thermally perturbed flows over a smooth mountain. However, simulations with small-scale topographic roughness tended to generate steadier, more elongated, and better-defined rainbands than corresponding simulations with only thermal perturbations. In the presence of both perturbation types, the only cases that developed quasi-stationary bands (Cases 1 and 2) were those that produced bands from thermal excitation alone. It appears that thermal perturbations traveling with the flow tend to disrupt any stationary and organized features forced by the roughened topography unless 1) the thermal perturbations are weak or 2) they take on similar structures as the topographically forced features themselves.

b. Relationship between small-scale topographic features and band structure

As just discussed, random small-scale roughness elements with a mean rms amplitude of just 30 m are sufficient to generate the banded and quasi-stationary structures in Cases 1 and 2. How do the bands that develop in response to such small bumps compare to those generated by larger isolated peaks such as those investigated by Cosma et al. (2002, hereafter CRM)? Consider the two simulations in Fig. 11 that are identical to the standard Case-2 simulation except that instead of random small-scale roughness, a 500-m-high

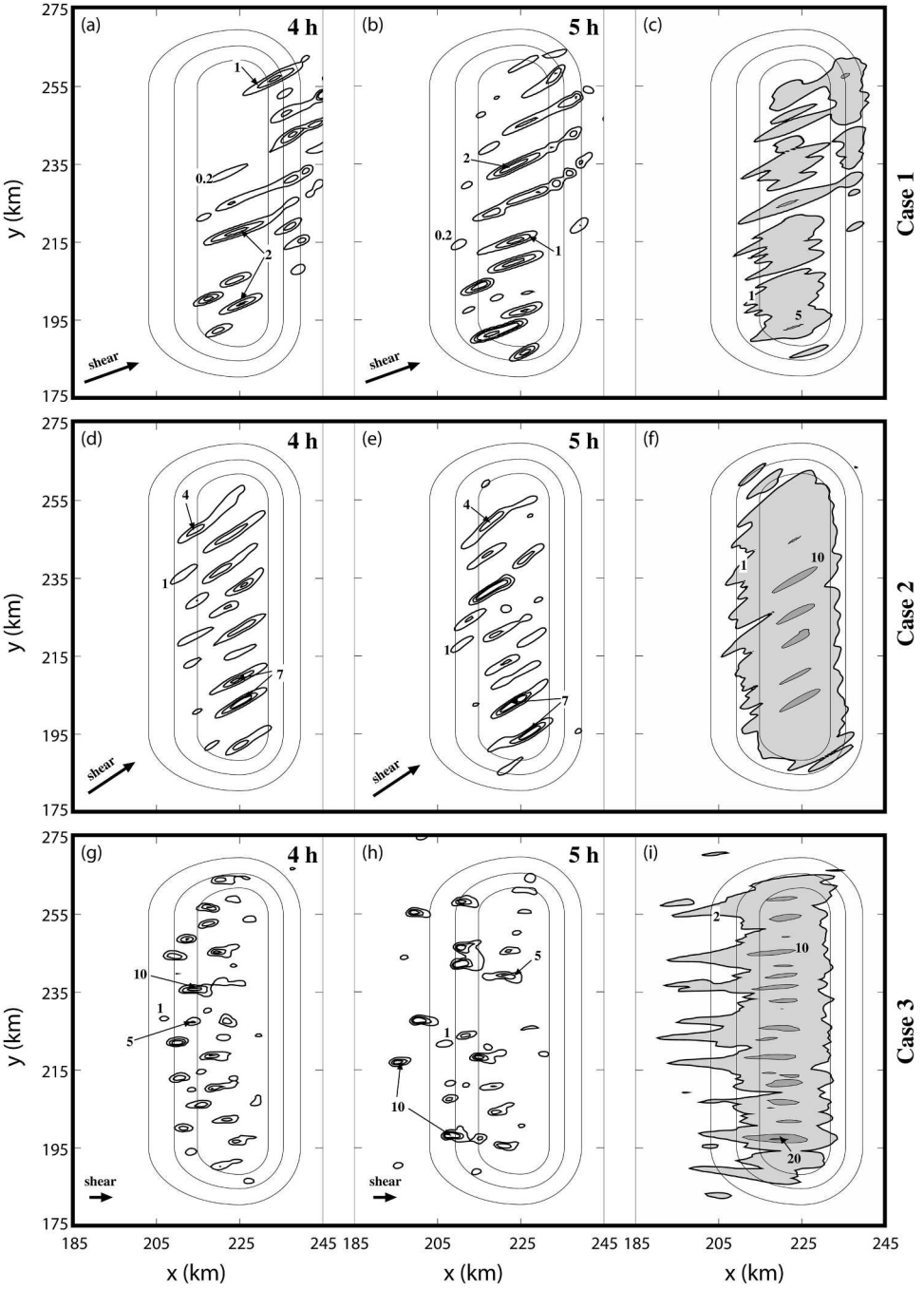

FIG. 9. As in Fig. 7, except that the topography does not contain small-scale random noise.

bump with a 2.5-km half-width is placed on the upwind slope of the ridge. Although the size of this bump is considerably smaller than the 1.2-km-high, 10-km-wide peaks simulated by CRM, it is representative of Mt. Hebo (see Fig. 1), the peak associated with rainband B5 in the radar observations of Case 2 (see Fig. 2c, d).

When this 500-m bump is added to the mountain at x = 210 km (Fig. 11a), the accumulated precipitation in its lee is much less than that produced by 30-m rms random topographic noise (Fig. 7f) and is only slightly enhanced compared to that which develops over a completely smooth mountain (Fig. 9f). In contrast, if the 500-m bump is moved just 15 km farther upstream, which is more representative of the location of Mt. Hebo relative to the main crest of Coastal Range, the bump creates a significant band of precipitation in its

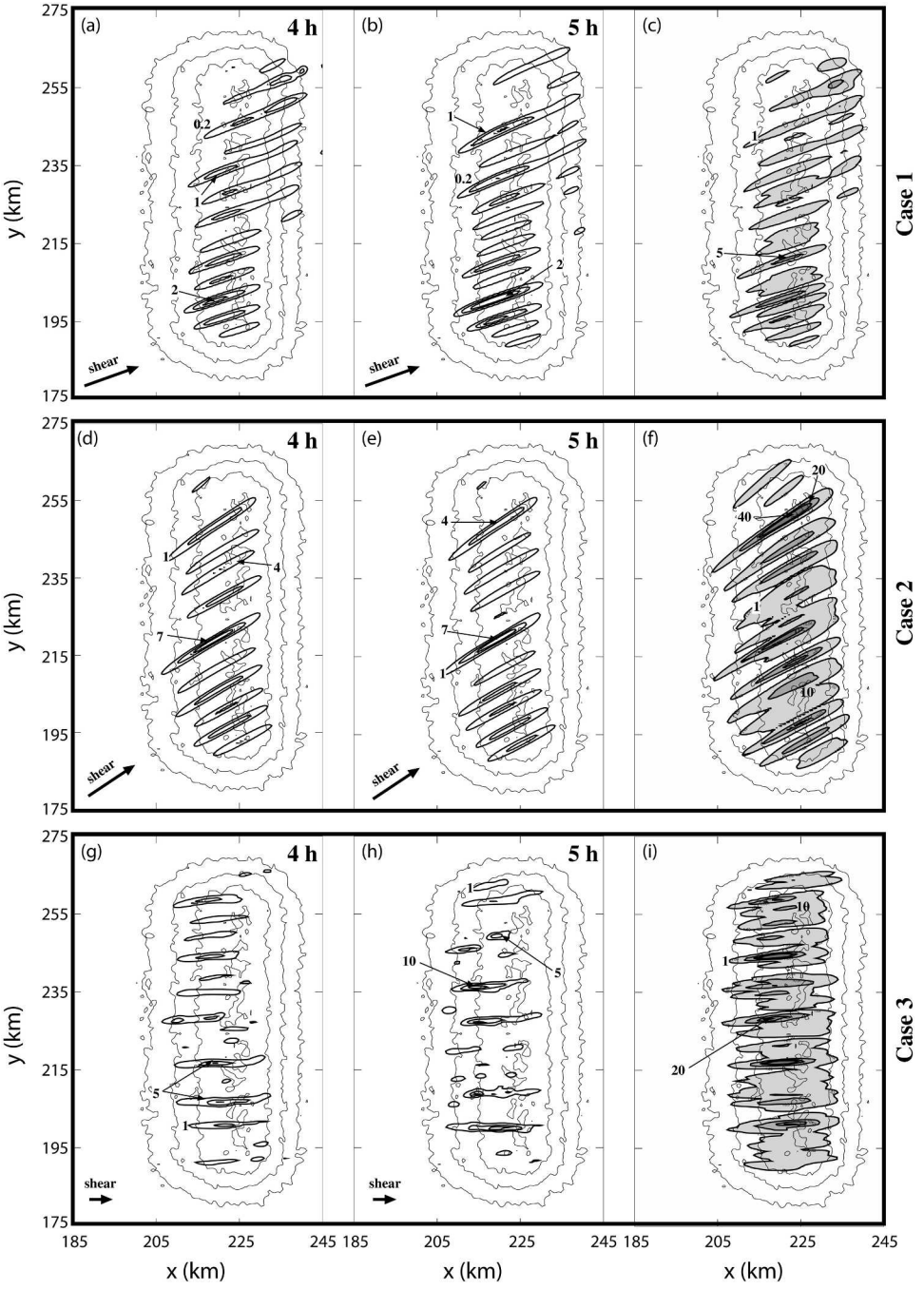

FIG. 10. As in Fig. 7, except that the thermal field does not contain small-scale perturbations.

lee, yet the maximum precipitation remains just slightly less than that produced by the 30-m rms random topography in rainband SB3 (Fig. 7f). If the bump is shifted even farther upstream (not shown), the band of enhanced precipitation gradually disappears, leaving surface accumulations that once again resemble the smooth mountain simulation. Similar results were obtained using 500-m-high bumps in Case 1, suggesting that 1) large isolated peaks are not necessarily more effective than a broad region of low-amplitude topographic roughness in generating banded orographic precipitation, and 2) the bands created by isolated peaks can be very sensitive to the location of those peaks relative to the main topographic ridge.

Given the effectiveness with which 30-m-rms topographic noise can generate bands in Cases 1 and 2, it is

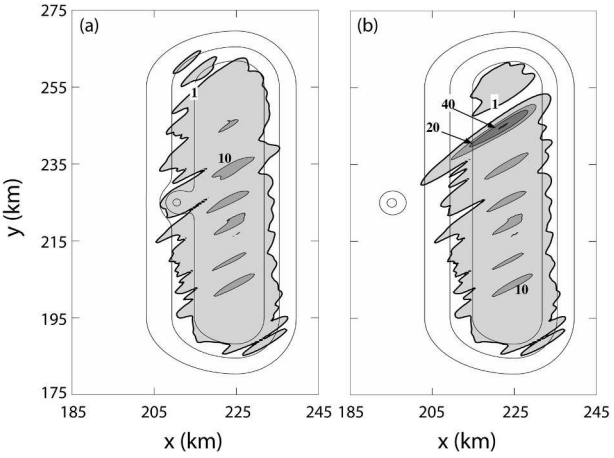

FIG. 11. Cumulative precipitation fields of simulations of Case 2 at $t = 5$ h over smooth topographies with added 500-m bump at $y = 225$ km and (a) $x = 210$ km and (b) $x = 195$ km. Precipitation contours are 1, 10, 20, and 40 mm; topographic contours are in intervals of 250 m.

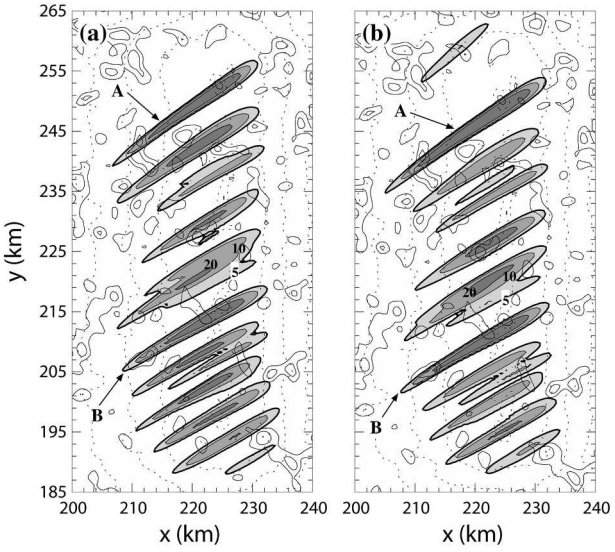

FIG. 12. Cumulative precipitation fields of simulations of Case 2 at $t = 5$ h with different topographic roughness fields. (a) Smoothed roughness field obtained by passing uniform noise field 12 times through diffusion operator. (b) Same as (a), but with noise field shifted 2 km to the south. Precipitation contours are 5, 10, and 20 mm; contours of underlying topography at 250-m intervals are shown by dashed line; positive perturbations in topographic noise field are given by solid lines at 30-m contour intervals.

reasonable to wonder how closely those bands are tied to the precise pattern of the random topographic noise. This question is addressed using a moderately smoother noise field than that considered in the previous simulations, which allows the roughness elements to be more clearly distinguished by the eye. This smoother noise field was created by passing the original noise field eight additional times through the aforementioned two-dimensional diffusion operator, then rescaling the perturbations to 30-m rms amplitude. One standard Case-2 simulation was conducted using this smoother noise field, along with a second otherwise identical simulation, in which the smoothed noise field was shifted 2 km to the south without altering the position of the finite-length ridge or the initial structure of the thermal perturbations. The 2-km shift, just slightly less than one-half wavelength, was chosen because it minimizes the differences in the flow impinging on the individual roughness elements due to the systematic variations in low-level winds produced by the larger-scale ridge that would accompany larger along-ridge shifts. The position of the resulting rainbands relative to the underlying topography is compared in Fig. 12. Almost all of the bands in Fig. 12b are shifted 2 km south of their position in Fig. 12a with only minimal changes in their size and intensity. Note in particular that the strong bands A and B very accurately maintain their position with respect to the underlying roughness field as that field is shifted to the south.

The strong influence of low-amplitude topographic irregularities on the location of orographic rainbands as revealed by the preceding comparison may help to explain the behavior of observed bands such as B4 in Fig. 2b and B8 in Figs. 2c,d, which persisted in quasi-stationary locations despite the lack of obvious small-scale topographic peaks in their immediate vicinity. Like the simulated bands in Figs. 7 and 12, these observed bands may have been fixed to small-scale features with amplitudes of less than 100 m, which are not clearly apparent in the topographic contours of Fig. 2. Further investigation is necessary to determine the physical mechanism by which low-amplitude topographic roughness is so effective at initiating and fixing the location of orographic rainbands.

6. Atmospheric influence on convective structure

While small-scale topographic features tend to increase the organization and steadiness of those orographic rainbands that develop in a given event, atmospheric properties appear to determine whether rainbands are preferred over more cellular structures as the primary mode of convective organization. Two such properties examined in this section are the background environment in the unstable orographic cap cloud and the atmospheric susceptibility to convection upstream of the mountain. Note that this is only a preliminary investigation into the factors that appear to affect bandedness in these cases, and a more thorough analysis of the physical mechanisms influencing the structure and propagation of shallow orographic convection will be deferred to a future investigation.

a. Background environment within the orographic cap cloud

In the comparisons of upstream flow parameters in Fig. 5 it was seen that all three cases exhibited similar

low-level potential instabilities and relative humidities. Thus as the air was lifted to saturation over the mountain upslope, the characteristic moist stabilities in the parent cap clouds of the three cases were very similar. On the other hand, the low-level wind speeds and shears in the upstream flow were clearly larger for Cases 1 and 2 than for Case 3 (Figs. 5c,d). Upon landfall, the near-surface wind speed was reduced to nearly zero by frictional dissipation, so that these differences in shear were further enhanced because of the stronger low-level winds in Cases 1 and 2.

The role of vertical shear in organizing buoyant convection has been addressed by numerous theoretical investigations (e.g., Kuo 1963; Hill 1968; Asai 1972; Sun 1978), all of which found that longitudinal bands aligned with the environmental shear vector are the preferred mode of convection for both dry and saturated statically unstable layers. Such shear-parallel convection has been observed in many different situations, including boundary layer roll vortices (Grossman 1982) and cloud streets (Malkus 1963), as well as tropical rainbands (Hildebrand 1998). Convective bands roughly aligned with the shear (and mean wind) vector have also been recently noted in observations (Yoshizaki et al. 2000) and numerical simulations (KD04) of shallow orographic convection. The numerical sensitivity tests performed by Yoshizaki et al. (2000) showed that stronger levels of low-level shear resulted in more elongated and organized convective bands.

The relationship between the vertical shear within the unstable cloud and the organization of convective rainbands in these numerical simulations is shown by plotting the mean shear vectors just upstream of the orographic cloud ($x = 185$ km and $y = 225$ km) over $0 \leq z \leq 2.5$ km, the approximate layer in which the clouds reside (see Fig. 8), on each of the q_r panels in Figs. 7, 9, and 10. Because the velocity is reduced to nearly zero magnitude at the surface, the directions of the mean wind and the vertical shear are essentially identical within this layer. In all three cases the rainbands are roughly parallel to the shear/wind vectors across the convective layer. The relatively strong vertical shears in Cases 1 and 2, whose absolute magnitudes at $t = 4$ h (0.0074 and 0.0072 s^{-1}) are nearly 3 times as large as that for Case 3 (0.0026 s^{-1}), appeared to have enhanced the banded structure of the convection.

b. Susceptibility to upstream convection

Two differences between Case 3 and the other two cases are apparent in both the radar images (Fig. 2) and the simulations (Fig. 7). In Case 3, precipitating convective cells form upstream of the mountain, and those rainbands that do occur over the mountain are shorter and less organized. These two differences appear to be related, because as disturbances initiate upstream and drift over the mountain, they disrupt the organization of any convective circulations that might otherwise form over the orography.

In order for moist convective cells to develop upstream of the cap cloud, some nonorographic source of upward motion is required to bring air parcels to their level of free convection (LFC). Frictional dissipation along the coastline, for one, decelerates the impinging flow, resulting in horizontal convergence and upward motion. While this coastal convergence undoubtedly brings the landfalling air mass closer to saturation, it fails to explain why cellular convection is initiated farther upstream in Case 3 than in Cases 1 and 2, in which the coastal convergence is greater because of stronger near-surface wind speeds. A possible source for local vertical motions that may explain these differences is the small-scale eddies initiated by thermal or mechanical perturbations in the planetary boundary layer. As described in section 4, such disturbances are represented in our simulations by a random initial field of thermal noise that is continually replenished at the upstream boundaries of the finest numerical grid. These buoyancy perturbations force dynamical responses that vary greatly depending on the static stability within the layer. For example, thermal perturbations in unstable layers yield amplifying circulations that can rapidly lift moist parcels to saturation and their LFC, while in strongly stable layers the majority of perturbation energy is radiated away by gravity waves. Thermal perturbations may also generate moist convection in weakly stable layers with high moisture content and low convective inhibition (CIN), where the reduced resistance to vertical ascent may allow sufficiently buoyant parcels to reach their LFC.

Figure 13 shows vertical profiles over the layer $0 \leq z \leq 1$ km of the static stability [defined as $N^2 = gd \ln\theta_v / dz$, where $\theta_v = \theta(1 + 0.61q_v)$], relative humidity, CIN,[1] and vertical distance to the LFC (Δz_{LFC}). The combination of comparatively low static stability below 0.5 km and high relative humidity above makes both the CIN and Δz_{LFC} for Case 3 much lower than that in the other cases. As a result of the weak stability, low CIN, and small Δz_{LFC}, buoyant perturbations rising from low levels in Case 3 can reach their LFC comparatively easily, which may explain the development convective cells upstream of the mountain in the observations and simulations of this event.

7. Conclusions

Operational radar observations and quasi-idealized numerical simulations have been used to examine

[1] Defined as

$$g \int_{z}^{\mathrm{LFC}} \{[T_v(z')]_p - [T_v(z')]_e\} / [T_v(z')]_e \, dz',$$

where $[T_v]_p$ and $[T_v]_e$ are the virtual temperatures of the displaced parcel and background environment, respectively. Note that CIN, which is usually defined as a single value corresponding to the surface, is calculated pointwise over the entire layer.

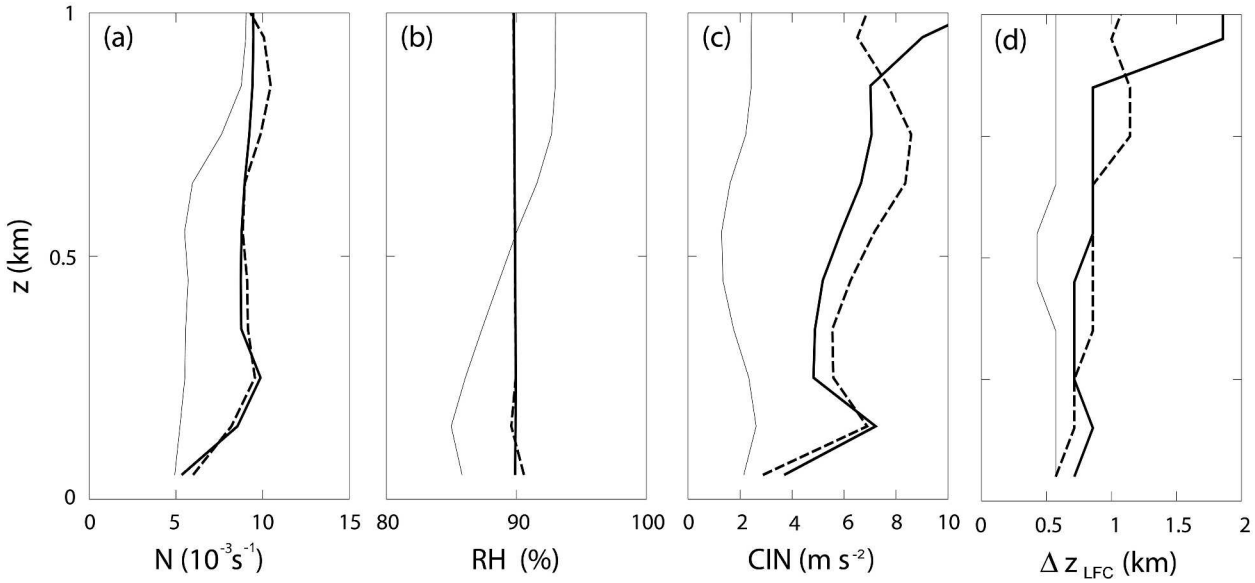

FIG. 13. Low-level thermodynamic profiles for Cases 1, 2, and 3: (a) N, (b) RH, (c) CIN, and (d) Δz_{LFC}. Case 1 is given by thick solid line, Case 2 by thick dashed line, and Case 3 by thin solid line.

banded convection in shallow orographic precipitation events over the Oregon Coastal Range. The convection in the three cases under consideration ranged from remarkably well-defined, organized, and steady rainbands (Case 2, 12–13 November 2002) to highly disorganized and cellular features (Case 3, 12 October 2003). Large localized precipitation enhancements occurred in the former case because of the steadiness of the convective bands.

The quasi-idealized numerical simulations, which used close approximations to the actual upstream flows and an idealized representation of the Coastal Range, were able to qualitatively reproduce the observed convection in the three events. As in the observations, a cellular convective pattern with only a few short bands formed in Case 3, while well-defined, quasi-stationary rainbands developed in Cases 1 and 2. These rainbands were located in the updraft regions of longitudinal roll circulations that formed within the unstable orographic cap cloud. Additional simulations revealed that the atmospheric structures impinging on the Coastal Range in Cases 1 and 2 were capable of supporting bands over smooth mountains without any small-scale peaks or roughness elements. Thus, in contrast to the previously investigated cases of shallow orographic convection in the Cévennes (Miniscloux et al. 2001) and in the Kyushu region of Japan (Yoshizaki et al. 2000), the potentially unstable cap cloud in Cases 1 and 2 was apparently subject to a roll-type instability even in the absence of subrange-scale peaks and valleys.

Although small-scale topographic irregularities were not necessary to produce rainbands in the simulations of Cases 1 and 2, the bands that formed in the presence of such topographic features were better organized and steadier than those forced only by thermal perturbations over smooth terrain. This increased stationarity resulted in substantial increases in localized precipitation accumulations. Two types of subrange-scale topographic perturbations were considered in the simulations: a random field of uniformly distributed roughness elements with 30-m rms amplitude and a single 500-m-high peak added to the mountain upslope. Consistent with the findings of Cosma et al. (2002), the isolated peak, when positioned optimally relative to the ridge crest, generated a pronounced stationary rainband in its lee, which may help to explain the large precipitation enhancements observed near Mt. Hebo in Case 2. This rainband, however, was highly sensitive to the location of the peak, and vanished as the peak was shifted 15 km closer to, or farther from, the crest. Despite its comparatively weak amplitude, the uniformly distributed topographic noise generated a very organized pattern of convective bands and enhanced the localized precipitation even beyond that of the 500-m peak. Evidently, prominent subrange-scale peaks are not necessarily more effective than low-amplitude roughness elements at triggering quasi-stationary orographic rainbands.

One key factor distinguishing the more banded cases (Cases 1 and 2) from the cellular case (Case 3) appears to have been an enhanced susceptibility to free convection upstream of the orographic cap cloud. This upstream convection, which was apparent in both observations and simulations of the event, was initiated by thermal perturbations in the less convectively inhibited Case-3 flow. Cells that formed in the upstream flow were advected through the orographic cloud and tended to disrupt rainband formation over the moun-

tain. The different levels of vertical shear within the parent orographic clouds may have also contributed to the varying levels of bandedness. The strong vertical shears in Cases 1 and 2, which were nearly 3 times greater than that in Case 3, helped to suppress any elongation of the cells in the cross-shear direction, resulting in a more organized pattern of shear-parallel bands. This was particularly evident in simulations over smooth terrain, where no topographic forcing existed to break the isotropy of the developing convection. In contrast, when the instabilities were triggered solely by roughened topography (in simulations without initial thermal perturbations), the differences in shear did not lead to difference in convective organization; all cases produced quasi-stationary bands. Finally, when both thermal and topographic perturbations were present, the simulated convective structures initiated by both mechanisms projected onto each other to produce bands in Cases 1 and 2, but failed to reinforce each other and produced disorganized convection in Case 3.

Acknowledgments. This material is based upon work supported by the National Science Foundation under Grants ATM-9979241 and ATM-0225441. We would like to express thanks to Mark Albright and David Ovens of the University of Washington Department of Atmospheric Sciences. Mark Albright led us to the rain gauge data over the Coastal Range; David Ovens's GEMPAK expertise was instrumental for our creation of Figs. 2 and 3. We also thank the anonymous reviewers for their insightful comments and suggestions.

REFERENCES

Anquetin, S., F. Miniscloux, J. D. Creutin, and S. Cosma, 2003: Numerical simulation of orographic rainbands. *J. Geophys. Res.,* **108D,** 8386, doi:10.1029/2002JD001593.

Asai, T., 1972: Thermal instability of a shear flow turning the direction with height. *J. Meteor. Soc. Japan,* **50,** 525–532.

Cosma, S., E. Richard, and F. Miniscloux, 2002: The role of small-scale orographic features in the spatial distribution of precipitation. *Quart. J. Roy. Meteor. Soc.,* **128,** 75–92.

Douglas, R. H., 1964: Hail size distributions. *Proc. World Conf. on Radio Meteorology and the 11th Weather Radar Conf.,* Boulder, CO, Amer. Meteor. Soc., 146–149.

Durran, D. R., and J. B. Klemp, 1983: A compressible model for the simulation of moist mountain waves. *Mon. Wea. Rev.,* **111,** 2341–2361.

Epifanio, C. C., and D. R. Durran, 2001: Three-dimensional effects in high-drag-state flows over long ridges. *J. Atmos. Sci.,* **58,** 1051–1065.

Grossman, R. L., 1982: An analysis of vertical velocity spectra obtained in the bomex fair-weather, trade-wind boundary layer. *Bound.-Layer Meteor.,* **23,** 323–357.

Hildebrand, P. H., 1998: Shear-parallel moist convection over the tropical ocean: A case study from February 1993 TOGA COARE. *Mon. Wea. Rev.,* **126,** 1952–1976.

Hill, G. E., 1968: On the orientation of cloud bands. *Tellus,* **20,** 132–137.

Kirshbaum, D. J., and D. R. Durran, 2004: Factors governing cellular convection in orographic precipitation. *J. Atmos. Sci.,* **61,** 682–698.

——, and ——, 2005: Atmospheric factors governing banded orographic convection. *J. Atmos. Sci.,* in press.

Kuo, H. L., 1963: Perturbations of plane couette flow in stratified fluid and origin of cloud streets. *Phys. Fluids,* **6,** 195–211.

Leveque, R. J., 1996: High-resolution conservative algorithms for advection in incompressible flow. *SIAM J. Numer. Anal.,* **33,** 627–665.

Lilly, D. K., 1962: On the numerical simulation of buoyant convection. *Tellus,* **14,** 148–172.

Malkus, J. S., 1963: Cloud patterns over tropical oceans. *Science,* **30,** 767–778.

Miniscloux, F., J. D. Creutin, and S. Anquetin, 2001: Geostatistical analysis of orographic rainbands. *J. Appl. Meteor.,* **40,** 1835–1854.

Sun, W.-Y., 1978: Stability analysis of cloud streets. *J. Atmos. Sci.,* **35,** 466–483.

Weckwerth, T. M., J. W. Wilson, R. M. Wakimoto, and N. A. Crook, 1997: Horizontal convective rolls: Determining the environmental conditions supporting their existence and characteristics. *Mon. Wea. Rev.,* **125,** 505–526.

Yoshizaki, M., T. Kato, Y. Tanaka, H. Takayama, Y. Shoji, and H. Seko, 2000: Analytical and numerical study of the 26 June 1998 orographic rainband observed in western Kyushu, Japan. *J. Meteor. Soc. Japan,* **78,** 835–856.

Zhang, D., and R. A. Anthes, 1982: A high-resolution model of the planetary boundary layer—Sensitivity tests and comparisons with SESAME-79 data. *J. Appl. Meteor.,* **21,** 1594–1609.